

## Self-Propulsion of a Volatile Drop on the Surface of an Immiscible Liquid Bath

Benjamin Reichert<sup>1</sup>, Jean-Benoît Le Cam<sup>1</sup>, Arnaud Saint-Jalmes<sup>1</sup>, and Giuseppe Pucci<sup>1,2,\*</sup>

<sup>1</sup>Université Rennes, CNRS, IPR (Institut de Physique de Rennes) UMR 6251, FR35000 Rennes, France

<sup>2</sup>CNR NANOTEC—Istituto di Nanotecnologia, S.S. di Cosenza, Ponte P. Bucci 33C, 87036 Rende, Italy



(Received 8 October 2020; revised 2 March 2021; accepted 24 August 2021; published 28 September 2021)

We demonstrate the self-propulsion of a volatile drop on the surface of a bath of an immiscible liquid. Evaporative heat pumping is converted into directed motion through thermocapillary stresses, which arise from the coupling between surface-tension-driven flows and temperature advection. A propulsive force arises from convection-sustained temperature gradients along the drop interface, resulting in a warmer pool of liquid being advected by the hydrodynamic flow in the underlying bath toward the back of the drop. The dependence of the drop speed on the activity source, i.e., the evaporation flux, is derived with scaling arguments and captures the experimental data.

DOI: 10.1103/PhysRevLett.127.144501

Drop evaporation is a key phenomenon in industrial and healthcare applications such as inkjet printing, aerosol dynamics, and disease transmission [1,2]. Evaporation is also involved in everyday life phenomena, as the levitation of droplets above a cup of hot tea [3,4], the Leidenfrost [5], and the coffee-stain effects [6]. When evaporation is forced by a hot substrate, drops may levitate [4,5,7] and even self-propel on the asymmetric vapor layer separating them from the substrate [8]. Drop self-propulsion may also occur in liquid bulk due to surface-tension gradients located at the drop's interface and known as Marangoni gradients [9]. These gradients usually have solutal origin and are often derived from theoretical postulates since they are difficult to probe [10–14]. The free surface of a liquid bath is a suitable platform for the self-propulsion of artificial bodies [15–19], including drops [20–22], and enables direct probing of flows [15,23,24] and concentration gradients [18]. Furthermore, recent works demonstrated that when a liquid-free surface hosts a volatile immiscible liquid, evaporation is spontaneously converted into Marangoni gradients [25,26].

In this Letter, we demonstrate that the evaporation of a volatile drop floating on a liquid bath is converted into drop propulsion. We benefit from the drop location at the interface to experimentally characterize the surface temperature field, and thus Marangoni gradients, hydrodynamic flows, and evaporation flux, which is the activity source. This allows us to rationalize the coupling between thermal transfers and hydrodynamic flows that govern self-propulsion. Evaporative cooling engenders thermocapillary stresses and propulsion is triggered by a thermocapillary convective instability. Asymmetric stresses emerge on the drop interface as a result of the nonlinear interplay between Marangoni flow and temperature advection, which spontaneously breaks the symmetry of the drop temperature field. Temperature gradients are convection sustained and give

rise to a propulsive force via the permanent advection of warmer liquid from the underlying bath toward the back of the drop.

The experimental system consists of a drop of volatile liquid (liquid 1) floating on a bath of immiscible liquid (liquid 2) (Fig. 1). We denote  $\rho_1$  ( $\rho_2$ ),  $\gamma_1$  ( $\gamma_2$ ), and  $\eta_1$  ( $\eta_2$ ) the density, surface tension, and dynamic viscosity of liquid 1 (liquid 2), respectively.  $\gamma_{12}$  is the interfacial tension between liquid 1 and 2. We tested different liquid pairs and drop sizes (Sec. I in [27]) and observed that all drops initially stay still for  $\sim 1$  min, then spontaneously set into motion with speed  $v \sim 0.01$ – $0.1$  mm s<sup>-1</sup>. As a result, it may take several minutes to detect the drop displacement with the naked eye. We focused on pancakelike drops with  $R \sim 1$  cm and  $h \sim 1$  mm, where  $h$  is the drop thickness (Fig. 1), the shape of which is due to the dominant effect of gravity with respect to capillarity [35]. The bath depth was fixed to  $H = 10$  cm.

We identified two propulsion behaviors differing in the trajectory's features. In the first, the drop motion is erratic with persistence length  $l \lesssim R$  [Fig. 1(a)], where  $l$  defines the typical distance over which the active particle loses information about its initial orientation [36]. In the second, the trajectory is straighter with  $l \gg R$  and the drop achieves a stationary speed after a transient acceleration phase [Fig. 1(c)]. The second behavior is observed when a film of liquid 2 coats the drop. This film substantially attenuates surface temperature fluctuations, which are responsible for the erratic motion in the first behavior (Sec. V and Supplemental Movies 1, 2 in [27]). The presence of the film thus makes the system more tractable both experimentally and theoretically.

We focus on the second type of behavior and choose the pair ethanol-silicone oil (liquid properties in Sec. I in [27]). Thermal imaging and particle tracking velocimetry (PTV) (Secs. III, IV in [27]) were used to characterize the system

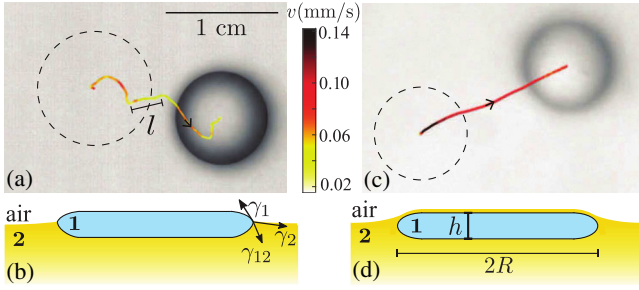


FIG. 1. Self-propulsion behaviors of volatile drops on liquid baths. First behavior: (a) the trajectory is erratic with  $l \lesssim R$  (top view) when the drop is in contact with air; (b) schematic side view, not to scale. Second behavior: (c) the trajectory is straighter with  $l \gg R$  (top view) when a film of liquid 2 covers the drop; (d) schematic side view. (a) Drop of 90% v/v ethanol in water. (c) Ethanol drop. (a),(c) Silicone oil bath with  $\eta_2 = 0.097$  Pa s.

temperature and velocity fields during the static [Figs. 2(a)–2(c)] and steady propulsion [Figs. 2(d)–2(f)] phases for  $\eta_2 = 0.097$  Pa s. Once the drop is deposited onto the bath, the silicone-oil film develops on its surface within  $\sim 100$  ms and ethanol pervaporates by diffusing through the film [Fig. 2(c)]. The drop cools down and displays axisymmetric flow and temperature fields [Figs. 2(a) and 2(b)], with

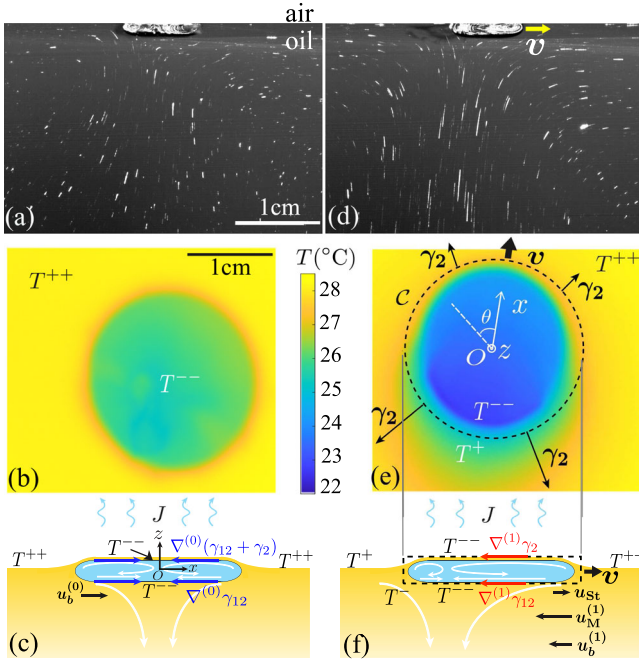


FIG. 2. Static symmetric (a)–(c) and propulsive asymmetric (d)–(f) state of an ethanol drop on a bath of silicone oil. (a),(d) Streamlines resulting from 15 sec of PTV (side view). (b),(e) Surface temperature field (top view), with  $T^{++} > T^+ > T^- > T^{--}$ . (c),(f) Side view schematics. White arrows indicate flows. Blue and red arrows indicate Marangoni stresses associated to base and perturbed flow, respectively. (e),(f) Dashed lines delimit the control volume used for the force balance. (a),(d)  $R = 4.0$  mm. (b),(e)  $R = 8.0$  mm.  $\eta_2 = 0.097$  Pa s.

average radial temperature gradient  $(T^{++} - T^{--})/R > 0$ , where  $T^{++} - T^{--} \simeq 5$  K [Figs. 2(b) and 2(c)].  $T^{++}$  and  $T^{--}$  denote the highest and lowest temperature in the system throughout its dynamics. Two inward flows develop close to the upper and lower interfaces and an outward flow develops in the drop's bulk [Figs. 2(a) and 2(c)]. Flow reversal occurs at the drop's axis of symmetry ( $Oz$ ). In the oil, the flow is inward near the drop's lower interface and deviates downward in the vicinity of the drop's axis of symmetry [Figs. 2(a) and 2(c)]. These flows are driven by interfacial stresses arising from the variation of interfacial tension with temperature along the radial direction. These Marangoni stresses are denoted  $\nabla^{(0)}(\gamma_{12} + \gamma_2)$  and  $\nabla^{(0)}\gamma_{12}$  for the upper and lower interfaces, respectively, and are directed toward the drop's center [Fig. 2(c)]. The index (0) refers to the flow generated by these stresses, which remains the base flow throughout the drop dynamics.

About one minute after drop deposition, thermal images reveal a symmetry breaking of the temperature field. A crescentlike cold patch with average temperature  $T^{--}$  appears in the vicinity of the drop horizontal contour [Fig. 2(e)]. The angular extension of the patch,  $\alpha$ , increases with time up to a stationary value  $\alpha_{\max}$  [Fig. 3(c)]. PTV shows that the zone of flow reversal shifts accordingly [Figs. 2(d) and 2(f)]. Correspondingly, the drop starts moving in the direction opposite to the displacement of the patch, along the average temperature gradient [ $\hat{x}$  direction in Figs. 2(e) and 2(f)].

In order to rationalize the mechanics of self-propulsion, we note that the Reynolds number comparing advection to viscous transport of momentum in the bath is  $\text{Re} = \rho_2 v R / \eta_2 \sim 10^{-2}$  with  $\eta_2 = 0.1$  Pa s. We thus use the Stokes equation and describe the global flow during the stationary propulsion [Figs. 2(d) and 2(f)] as the superposition of an order (0) symmetric flow and an order (1) perturbation flow. The order (1) flow is associated to the average temperature difference  $\Delta T = T^{++} - T^+ \simeq 1$  K between the fore and the aft of the drop.  $\Delta T$  induces Marangoni stresses at the upper and lower interfaces that drag liquid from the fore to the aft, and are responsible for the displacement of the region of flow reversal [Fig. 2(f)].

We develop our model in the laboratory frame of reference. In order to derive a scaling law for the drop stationary speed, we consider the  $x$  component of the forces experienced by a cylindrical control volume of radius  $R$  and thickness  $h$  containing the drop [Figs. 2(e) and 2(f)]. These forces arise as a result of the perturbative flow outside the drop, which is the sum of two flows [Fig. 2(f)].

The first flow is the Stokes flow associated with the motion of a viscous disc in a quiescent fluid without Marangoni effect [37,38]. This yields the Stokes viscous drag  $F_{\text{St}} \sim -\eta_2 R v_s < 0$  [39], with constant prefactor as  $(h/R), (\eta_1/\eta_2) \ll 1$  [37,38,40]. We denote  $u_{\text{St}} > 0$  the characteristic velocity of the Stokes flow in the  $\hat{x}$  direction close to the lower interface in liquid 2 [Fig. 2(f)].

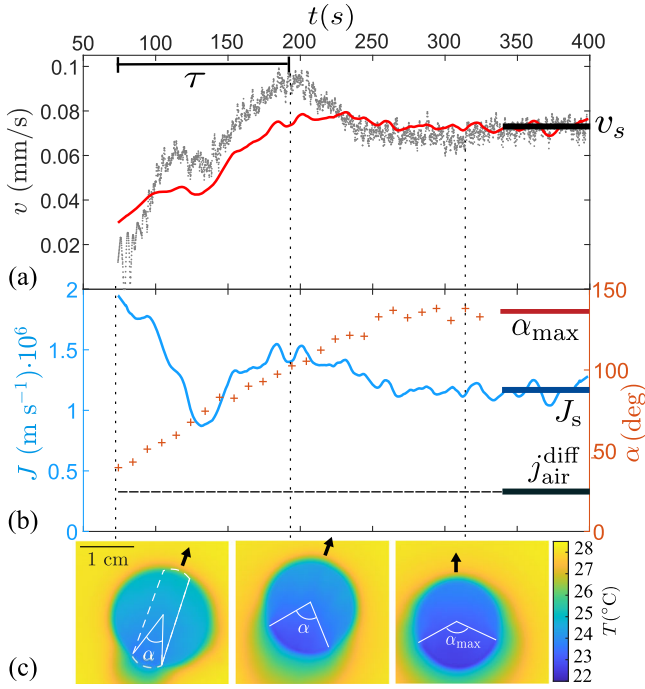


FIG. 3. Time evolution of drop speed, evaporation flux, and temperature field. (a) Experimental drop speed  $v(t)$  (full circles), with  $v_s$  the stationary speed. The solid line results from (5) combined with the evaporation flux  $J(t)$  in (b). (b) Experimental evaporation flux  $J(t)$  (solid line) and angular extension  $\alpha(t)$  (plus symbol) of the cold patch.  $J_s$  is the stationary evaporation flux and  $\alpha_{\max}$  is the maximum angle.  $j_{\text{air}}^{\text{diff}}$  is the diffusive evaporation flux of an ethanol disk with radius  $R$ . (c) Temporal evolution of the surface temperature field (Supplemental Movie 1 [27]). The dashed line delimits the upper side of the control volume in the transient regime.  $R = 8.0$  mm,  $\eta_2 = 0.097$  Pa s.

The second flow is due to the Marangoni stresses at the interface of a drop that is at rest with respect to the bath. We denote  $\nabla^{(1)}\gamma_2$  and  $\nabla^{(1)}\gamma_{12}$  the gradients at the upper and lower interfaces, respectively, which generate two forces. A first force is the result of the inhomogeneous, radial, and outwardly pulling tension  $\gamma_2[T(\theta)]$  due to azimuthal temperature variations. It applies to the closed contour  $C$  [Fig. 2(e)] and reads

$$F_{\text{cam}} = \oint_C \gamma_2 \cdot \hat{\mathbf{x}} dl = \int_S \nabla^{(1)}\gamma_2 \cdot \hat{\mathbf{x}} dS \sim -\frac{|d\gamma/dT|\Delta T}{R} \pi R^2, \quad (1)$$

where  $S$  is the area of the upper side of the control volume [Fig. 2(e)]. Here and in the following we assume  $|d\gamma/dT| \sim |d\gamma_2/dT| \sim |d\gamma_{12}/dT|$  [41] (Sec. I [27]).  $F_{\text{cam}}$  is the thermal analog of the force that drives camphor boats towards zones with lower surfactant concentration [42], but here  $F_{\text{cam}} < 0$  opposes the drop motion.

A second force results from the Marangoni stress  $\nabla^{(1)}\gamma_{12}$  at the drop's lower interface, which induces a viscous stress response in the underlying bath that is oriented in the drop's direction of motion. The drop gains traction from the bath in order to propel. We denote  $u_M^{(1)} < 0$  the characteristic velocity of the perturbed flow in the  $\hat{\mathbf{x}}$  direction close to the lower interface in liquid 2 [Fig. 2(f)]. This flow produces a strain rate  $\sim |u_M^{(1)}|/R$  [43] and the resulting force on the lower side of the control volume reads

$$F_{\text{prop}} \sim \eta_2 \frac{|u_M^{(1)}|}{R} \cdot \pi R^2. \quad (2)$$

The problem is thus reduced to computing  $u_M^{(1)}$ . In our experiments, viscous stress inside the drop is negligible with respect to its counterpart in the outer liquid,  $\eta_1/h \ll \eta_2/R$ . Therefore, the continuity of stresses at the lower interface yields  $u_M^{(1)} \sim -|d\gamma/dx|R/\eta_2 \sim -|d\gamma/dT|\Delta T/\eta_2$  (Sec. VI in [27]). Substituting this expression in (2) we obtain  $F_{\text{prop}} \sim |d\gamma/dT|\Delta TR > 0$ .  $F_{\text{prop}}$  has the same scaling as  $F_{\text{cam}}$ , but opposite direction. Since the drop is moving in the direction of  $F_{\text{prop}}$ , we may write  $F_{\text{prop}} + F_{\text{cam}} \sim |d\gamma/dT|\Delta TR > 0$ . A scaling for the stationary speed is derived by balancing this expression with  $F_{\text{St}}$ , which yields

$$v_s \sim \left| \frac{d\gamma}{dT} \right| \frac{\Delta T}{\eta_2}. \quad (3)$$

In order to derive a scaling for  $\Delta T$ , we analyze how evaporation energy is converted into liquid motion. We simultaneously measured the drop speed  $v(t)$ , the angular extension of the cold patch  $\alpha(t)$ , and the evaporation flux  $J(t)$  for drop volume  $V = 0.4$  ml and  $\eta_2 = 0.097$  Pa s (Fig. 3). The drop is deposited on the bath at  $t = 0$  s and starts moving at  $t = 74$  s. After a transient regime of acceleration, the drop achieves a stationary speed  $v_s$ . We measure  $J(t) = -dV(t)/dt/A(t)$ , where  $A(t) = \pi R^2(t)$  is the area and  $V(t) = hA(t)$  is the drop volume (Sec. II [27]).  $v(t)$ ,  $\alpha(t)$  and  $J(t)$  exhibit similar timescales of evolution toward the stationary regime, which suggests that  $v(t)$  is correlated to  $\alpha(t)$  and  $J(t)$ .

We focus on the stationary regime and calculate how  $v_s$  scales with the thermal evaporation flux,  $\rho_1 \mathcal{L}_v J_s$ , where  $\mathcal{L}_v$  is the latent heat of evaporation of ethanol. We perform a thermal flux balance to relate  $\Delta T$  to the heat flux of evaporation.  $u_b^{(1)} = u_M^{(1)} + u_{\text{St}} < 0$  is the characteristic velocity of the perturbed flow in the  $\hat{\mathbf{x}}$  direction. Heat transport in the bath is governed by two processes, convection and diffusion, the relative importance of which is quantified by a thermal Péclet number for each component of the flow,  $\text{Pe}^{(0)} = Ru_b^{(0)}/D_{\text{th}}$  and  $\text{Pe}^{(1)} = Ru_b^{(1)}/D_{\text{th}}$ .  $D_{\text{th}} = \lambda_2/\rho_2 C_p$  is the thermal diffusion coefficient, with  $C_p$  and  $\lambda_2$  the

thermal capacity and conductivity of silicone oil. For  $R \approx 8$  mm and measured velocities  $u_b^{(0)} \approx 0.13$  mm s<sup>-1</sup> and  $u_b^{(1)} \approx 0.05$  mm s<sup>-1</sup>  $\approx$  for  $\eta_2 = 0.097$  Pa.s, we obtain  $\text{Pe}^{(0)} \approx 9$  and  $\text{Pe}^{(1)} \approx 4$ , which suggest that convection is dominant. The temperature difference  $\Delta T$  is sustained by the cooling of fluid particles that move backward in the vicinity of the drop's upper interface, driven by the thermal evaporative flux  $\rho_1 \mathcal{L}_v J_s$ . This temperature difference induces thermal convection in the underlying bath,  $\rho_2 C_p \Delta T |u_b^{(1)}|$ , from the fore towards the aft of the drop. The heat flux balance reads

$$\rho_2 C_p \Delta T |u_b^{(1)}| = c \rho_1 \mathcal{L}_v J_s, \quad (4)$$

where  $c$  represents the fraction of thermal evaporation flux that is converted into the convective heat flux of the perturbed flow. By substituting  $u_b^{(1)} \approx 0.05$  mm s<sup>-1</sup>,  $J_s = 1.2 \times 10^{-6}$  m s<sup>-1</sup> and  $\Delta T \approx 1$  K from experiments in (4), we found  $c = 0.08$ , which suggests that the evaporation flux is not modified by the drop propulsion at leading order. Furthermore, we note that  $u_{\text{St}} \sim v_s$  for Stokes flow past a viscous body in the limit  $\eta_1/\eta_2 \ll 1$  [39]. Since  $u_M^{(1)}$  and  $v_s$  have the same scaling [cf. (3)] then  $u_b^{(1)} \sim -|d\gamma/dT| \Delta T / \eta_2$ . We thus obtain  $\Delta T \sim [\eta_2 \rho_1 \mathcal{L}_v J_s / \rho_2 C_p |d\gamma/dT|]^{1/2}$ , that combined with (3) yields the scaling of the drop stationary speed with the stationary evaporation flux  $v_s \sim [\rho_1 |d\gamma/dT| \mathcal{L}_v J_s / \rho_2 \eta_2 C_p]^{1/2}$ .

We now focus on the transient regime, characterized by an increasing angular extension  $\alpha(t)$  of the cold crescent over the typical time  $\tau \sim 100$  s [Figs. 3(b) and 3(c)]. Since  $\tau$  is much larger than the timescale of the viscous diffusion of momentum in the bath,  $\tau_v = \rho_2 R^2 / \eta_2 \sim 1$  s, we consider the velocity field in the bath as quasistationary. Consequently, the scaling of  $v_s$  can be extended to the transient regime by considering a geometrical factor  $g[\alpha(t)]$  that takes into account the time evolution of the cold crescentlike patch [Fig. 3(c)]. During the transient regime,  $\nabla^{(1)} \gamma_2$  and  $\nabla^{(1)} \gamma_{12}$  apply to the area  $S_{\text{tr}}(\alpha) = 2g(\alpha)R^2$  at the upper and lower side, respectively, of a time-varying control volume with  $g(\alpha) = \alpha/2 + \cos(\alpha/2) \sin(\alpha/2)$ .  $S_{\text{tr}}$  is a fraction of the total drop surface  $\pi R^2$  and its contour is represented in Fig. 3(c). A force balance on the time-varying control volume gives

$$v(t) = \beta g(\alpha) \left[ \frac{\rho_1 |d\gamma/dT| \mathcal{L}_v J(t)}{\rho_2 \eta_2 C_p} \right]^{1/2}. \quad (5)$$

Using the experimental  $J(t)$  in Fig. 3(b) this expression yields a reasonable fit to the experimental speed with  $\beta = 0.087$  [red line in Fig. 3(a)]. For  $\alpha = \alpha_{\text{max}}$  we recover the stationary regime.

We now elucidate the nature of the activity source, i.e., the evaporation flux  $J$ . Drop evaporation is limited by vapor

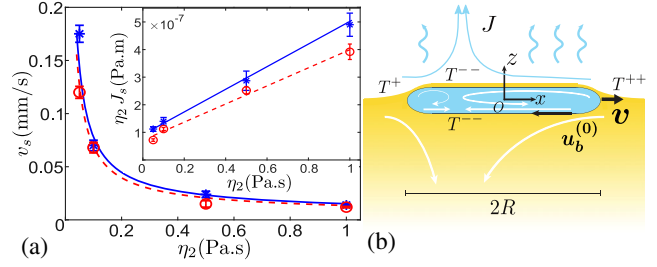


FIG. 4. Relation between drop speed  $v_s$  and evaporation flux  $J_s$  in the stationary regime. (a)  $v_s$  vs bath viscosity  $\eta_2$ . Lines represent the scaling in (6) combined with the fits in the inset. Inset: lines represent fits of  $a\eta_2 + b$ .  $R = 4.0$  mm: (star symbol), continuous lines and  $(a, b) = (4.1 \times 10^{-7}$  m s<sup>-1</sup>,  $9.2 \times 10^{-8}$  m Pa).  $R = 8.0$  mm: (“o” symbol), dashed lines and  $(a, b) = (3.3 \times 10^{-7}$  m s<sup>-1</sup>,  $7.1 \times 10^{-8}$  m Pa). (b) Side view schematic. White arrows indicate flows.

transport in air. The measured evaporation flux exceeds the diffusive flux of evaporation of an ethanol disk with radius  $R$ ,  $j_{\text{air}}^{\text{diff}} = 4D_1 \rho_{\text{sat}} / \pi R \rho_1$  [44], where  $\rho_{\text{sat}}$  is the saturation vapor density and  $D_1$  is the diffusion coefficient of ethanol in air [Fig. 3(b)]. This suggests that both diffusion and convection are involved in the evaporation process [Fig. 4(b)]. The magnitude of the evaporative flux is determined by the order (0) flows associated to the temperature difference  $T^{++} - T^{--} \approx 5$  K, which differs by no more than 1 K across bath viscosities. Convection in the air is driven by the drop upper interfacial flow, the speed of which can be tuned by varying the bath viscosity  $\eta_2$ . We measured the variation of  $J_s$  and  $v_s$  with  $\eta_2$  for drops with radii  $R = 4.0$  mm and  $R = 8.0$  mm (Fig. 4).  $\eta_2 J_s$  is an affine function of  $\eta_2$  [inset Fig. 4(a)], thus  $J_s = a + b/\eta_2$ . We identify  $a$  as the diffusive term and  $b/\eta_2$  as the convective term. Their decoupling is typical for mass or heat transfer from a body immersed in a flow with low Re and Pe up to  $\mathcal{O}(1)$  [45]. The order of magnitude of the fitting parameter  $a$  [Fig. 4(a)] is captured by  $j_{\text{diff}}^{\text{air}} = \{6.4 \times 10^{-7}; 3.2 \times 10^{-7}\}$  m s<sup>-1</sup> for  $R = \{4.0; 8.0\}$  mm. The term  $b/\eta_2$  results from a nontrivial coupling between the inner and outer flow through Marangoni stresses at the drop interface (Sec. VII [27]). The dependence on  $1/\eta_2$  is a signature of the dominant effect of outer shear stress over inner drop recirculation on the interfacial velocity for  $\eta_2 \gg \eta_1$ . The combination of the fit  $J_s = a + b/\eta_2$  with (5) with fixed  $\beta = 0.087$  and  $g(\alpha_{\text{max}})$  yields

$$v_s = \beta g(\alpha_{\text{max}}) \left[ \frac{\rho_1 |d\gamma/dT| \mathcal{L}_v (a + b/\eta_2)}{\rho_2 \eta_2 C_p} \right]^{1/2}, \quad (6)$$

which captures the dependence of the stationary speed on bath viscosity [Fig. 4(a)]. This result demonstrates that both diffusion and convection are involved in the drop activity. Furthermore, Eq. (6) captures the experimental data for both radii. The dependence of drop speed on the radius is

contained in the evaporative flux  $J_s$ , which decreases with  $R$ . This is discussed in detail in the Supplemental Material along with the dependence of self-propulsion on bath depth (Secs. VIII, IX in [27]).

We investigated the spontaneous motion of a volatile drop on a liquid bath. This system allows direct probing of the physical origin of surface-tension gradients, which is quite unique in the context of active drops [11–13] and has allowed us to rationalize the propulsion mechanism. A propulsive force results from Marangoni stresses that arise at the drop's lower interface from convection-sustained temperature gradients. The direction of motion is opposite to the interfacial tension gradients and thus to a Marangoni surfer [17,42,46]. Since the drop develops tangential stresses in order to propel, it can be considered a two-dimensional squirmer [47–49]. A recent work has shown that the combination of evaporation-induced wetting transition and Marangoni stresses of solutal origin triggers the spontaneous emulsification of a volatile drop on the surface of a liquid bath [26]. Spontaneous emulsification and self-propulsion are the two essential ingredients for the design of interfacial active emulsions [49].

B. R. and G. P. thank the program CNRS Momentum for its support. The authors thank Isabelle Cantat and Adrien Bussonnière for useful discussions.

\*Corresponding author.

giuseppe.pucci@cnr.it

- [1] D. Zang, S. Tarafdar, Y. Y. Tarasevich, M. D. Choudhury, and T. Dutta, *Phys. Rep.* **804**, 1 (2019).
- [2] W. C. Poon, A. T. Brown, S. O. Direito, D. J. Hodgson, L. Le Nagard, A. Lips, C. E. MacPhee, D. Marenduzzo, J. R. Royer, A. F. Silva *et al.*, *Soft Matter* **16**, 8310 (2020).
- [3] V. J. Schaefer, *Am. Sci.* **59**, 534 (1971).
- [4] V. S. Ajaev and O. A. Kabov, *Annu. Rev. Fluid Mech.* **53**, 203 (2021).
- [5] J. G. Leidenfrost, *De Aquae Communis Nonnullis Qualitatibus Tractatus* (Ovenius, Duisburg, 1756).
- [6] R. D. Deegan, O. Bakajin, T. F. Dupont, G. Huber, S. R. Nagel, and T. A. Witten, *Nature (London)* **389**, 827 (1997).
- [7] D. Quéré, *Annu. Rev. Fluid Mech.* **45**, 197 (2013).
- [8] A. Bouillant, T. Mouterde, P. Bourrienne, A. Lagarde, C. Clanet, and D. Quéré, *Nat. Phys.* **14**, 1188 (2018).
- [9] Y. S. Ryazantsev, M. G. Velarde, R. G. Rubio, E. Guzmán, F. Ortega, and P. López, *Adv. Colloid Interface Sci.* **247**, 52 (2017).
- [10] T. Toyota, H. Tsuha, K. Yamada, K. Takakura, T. Ikegami, and T. Sugawara, *Chem. Lett.* **35**, 708 (2006).
- [11] S. Thutupalli, R. Seemann, and S. Herminghaus, *New. J. Phys.* **13**, 073021 (2011).
- [12] Z. Izri, M. N. van der Linden, S. Michelin, and O. Dauchot, *Phys. Rev. Lett.* **113**, 248302 (2014).
- [13] C. C. Maass, C. Krüger, S. Herminghaus, and C. Bahr, *Annu. Rev. Condens. Matter Phys.* **7**, 171 (2016).
- [14] M. Morozov and S. Michelin, *J. Fluid Mech.* **860**, 711 (2019).
- [15] A. Snezhko, M. Belkin, I. S. Aranson, and W.-K. Kwok, *Phys. Rev. Lett.* **102**, 118103 (2009).
- [16] S. K. Chung, K. Ryu, and S. K. Cho, *Appl. Phys. Lett.* **95**, 014107 (2009).
- [17] N. J. Suematsu, S. Nakata, A. Awazu, and H. Nishimori, *Phys. Rev. E* **81**, 056210 (2010).
- [18] Y. Karasawa, S. Oshima, T. Nomoto, T. Toyota, and M. Fujinami, *Chem. Lett.* **43**, 1002 (2014).
- [19] G. Grosjean, G. Lagubeau, A. Darras, M. Hubert, G. Lumay, and N. Vandewalle, *Sci. Rep.* **5**, 16035 (2015).
- [20] Y. Couder, S. Protiere, E. Fort, and A. Boudaoud, *Nature (London)* **437**, 208 (2005).
- [21] G. Pucci, *Int. J. Nonlinear Mech.* **75**, 107 (2015).
- [22] E. Bormashenko, Y. Bormashenko, R. Gryniov, H. Aharoni, G. Whyman, and B. P. Binks, *J. Phys. Chem. C* **119**, 9910 (2015).
- [23] J. W. Bush and D. L. Hu, *Annu. Rev. Fluid Mech.* **38**, 339 (2006).
- [24] H. Ebata and M. Sano, *Sci. Rep.* **5**, 8546 (2015).
- [25] D. Yamamoto, C. Nakajima, A. Shioi, M. P. Krafft, and K. Yoshikawa, *Nat. Commun.* **6**, 7189 (2015).
- [26] L. Keiser, H. Bense, P. Colinet, J. Bico, and E. Reyssat, *Phys. Rev. Lett.* **118**, 074504 (2017).
- [27] See Supplemental Material at <http://link.aps.org/supplemental/10.1103/PhysRevLett.127.144501> for liquid properties, details on the experimental setup and further theoretical developments. Thermal and PTV videos are also included. It includes Refs. [28–34].
- [28] Y. Fukatani, D. Orejon, Y. Kita, Y. Takata, J. Kim, and K. Sefiane, *Phys. Rev. E* **93**, 043103 (2016).
- [29] J. G. Speight, *Lange's Handbook of Chemistry* (McGraw-Hill Education, New York, 2017).
- [30] L. Girifalco and R. J. Good, *J. Phys. Chem.* **61**, 904 (1957).
- [31] J. Sebilliau, *Langmuir* **29**, 12118 (2013).
- [32] L. Champougny, M. Roché, W. Drenckhan, and E. Rio, *Soft Matter* **12**, 5276 (2016).
- [33] D. Chuan and F. Yurun, *Chin. J. Chem. Eng.* **19**, 205 (2011).
- [34] K. Sefiane, J. Moffat, O. Matar, and R. Craster, *Appl. Phys. Lett.* **93**, 074103 (2008).
- [35] P.-G. De Gennes, F. Brochard-Wyart, and D. Quéré, *Capillarity and Wetting Phenomena* (Springer Science & Business Media, New York, 2013).
- [36] A. Zöttl and H. Stark, *J. Phys. Condens. Matter* **28**, 253001 (2016).
- [37] J. Hadamard, *C.R. Hebd. Seances Acad. Sci.* **152**, 1735 (1911).
- [38] W. Rybczynski, *Bull. Acad. Sci. Cracovie A* **1**, 40 (1911).
- [39] E. Guyon, J.-P. Hulin, L. Petit, C. D. Matescu *et al.*, *Physical Hydrodynamics* (Oxford University Press, New York, 2001).
- [40] S. Kim and S. J. Karrila, *Microhydrodynamics: Principles and Selected Applications* (Butterworth-Heinemann, 1991).
- [41] L. Girifalco and R. J. Good, *J. Phys. Chem.* **61**, 904 (1957).
- [42] S. Nakata and K. Matsuo, *Langmuir* **21**, 982 (2005).
- [43] M. Schmitt and H. Stark, *Phys. Fluids* **28**, 012106 (2016).
- [44] J. Crank, *The Mathematics of Diffusion* (Oxford University Press, New York, 1979).

- [45] A. Acrivos and T. D. Taylor, *Phys. Fluids* **5**, 387 (1962).  
[46] E. Lauga and A. M. Davis, *J. Fluid Mech.* **705**, 120 (2012).  
[47] M. Lighthill, *Commun. Pure Appl. Math.* **5**, 109 (1952).  
[48] J. R. Blake, *J. Fluid Mech.* **46**, 199 (1971).  
[49] S. Herminghaus, C. C. Maass, C. Krüger, S. Thutupalli, L. Goehring, and C. Bahr, *Soft Matter* **10**, 7008 (2014).